九州大学学術情報リポジトリ
Kyushu University Institutional Repository

High mobility of (111)-oriented large-domain (>100 μm) poly-InSb on glass by rapid-thermal crystallization of sputter-deposited films

Kajiwara, Takashi
Department of Electronics, Kyushu University

Shimoda, Otokichi
Faculty of Engineering, University of the Ryukyus

Okada, Tatsuya
Faculty of Engineering, University of the Ryukyus

Charith Jayanada Koswaththage
Faculty of Engineering, University of the Ryukyus

他

https://hdl.handle.net/2324/7172265

出版情報：Journal of Applied Physics. 132, pp.145302-, 2022-10-11. AIP Publishing
バージョン：
権利関係：© 2022 Author(s).

Journal of Applied Physics ARTICLE scitation.org/journal/jap

High mobility of (111)-oriented large-domain (>100 μm) poly-InSb on glass by rapid-thermal crystallization of sputter-deposited films

Cite as: J. Appl. Phys. **132**, 145302 (2022); doi: 10.1063/5.0105045
Submitted: 22 June 2022 · Accepted: 14 September 2022 ·
Published Online: 11 October 2022

View Online

Export Citation

CrossMark

Takashi Kajiwara,[1,a)] Otokichi Shimoda,[2] Tatsuya Okada,[2] Charith Jayanada Koswaththage,[2] Takashi Noguchi,[2] and Taizoh Sadoh[1,b)]

AFFILIATIONS

[1]Department of Electronics, Kyushu University, 744 Motooka, Fukuoka 819-0395, Japan
[2]Faculty of Engineering, University of the Ryukyus, 1 Senbaru, Okinawa 903-0213, Japan

[a)]**Electronic mail:** t.kajiwara@et.kyushu-u.ac.jp
[b)]**Author to whom correspondence should be addressed:** sadoh@ed.kyushu-u.ac.jp

ABSTRACT

Rapid-thermal annealing (RTA) of InSb precursor films, deposited by sputtering using an Ar plasma at room temperature, has been investigated to achieve high carrier mobility on low-cost glass substrates. Although InSb films containing residual Ar (∼1%) were partially lost by evaporation during RTA, such evaporation during RTA is suppressed by reducing the residual Ar to ∼0.3%. The crystallinity of the films is significantly increased by RTA at temperatures above 400 °C. The electron mobilities of the films increase with increasing RTA temperature up to 490 °C, showing the maximum values (9000–10 000 $cm^2 V^{-1} s^{-1}$) at 490 °C, and then, the mobilities decrease at RTA temperatures above 490 °C. The mobilities of 9000–10 000 $cm^2 V^{-1} s^{-1}$ are obtained for films with a wide range of thickness (300–1000 nm) grown at 490 °C. Detailed analysis indicated that the high carrier mobilities are realized by preferentially (111)-oriented large crystal domains (diameter: >100 μm), obtained by the regrowth of randomly oriented small grains, together with a low barrier height (16 meV) at the sub-domain boundaries (twin boundaries) in the large domains. The RTA after the sputtering technique will facilitate high-performance InSb-based devices with low production costs.

Published under an exclusive license by AIP Publishing. https://doi.org/10.1063/5.0105045

I. INTRODUCTION

Indium antimonide (InSb) shows the highest carrier mobility (∼70 000 $cm^2 V^{-1} s^{-1}$ for single crystals at 300 K) and the narrowest bandgap (0.18 eV at 300 K) among various semiconductors.[1] In addition, InSb has a large electron g factor and strong spin–orbit interaction.[2] Due to these remarkable properties, InSb is an attractive material for high-sensitivity magnetic sensors[3–8] and high-efficiency infrared detectors,[9–13] as well as high-speed transistors[14–17] and quantum computing devices.[18–21] However, almost all of the InSb devices have been fabricated using single-crystal InSb wafers or InSb layers epitaxially grown on single-crystal substrates,[22–25] which increases the production cost and limits the applications. To decrease the production cost of InSb devices, a growth process of high-quality InSb films on low-cost substrates, such as glass, should be developed. In addition, a sputtering technique should be employed for the deposition of the films, instead of high-cost epitaxy techniques such as liquid-phase epitaxy and molecular beam epitaxy.

Recently, Koswaththage *et al.* reported crystallization of InSb films (thickness: 1 μm) on glass substrates by rapid-thermal annealing (RTA), where the grown films showed high mobility (25 000 $cm^2 V^{-1} s^{-1}$).[26] However, they employed a vacuum evaporation method for InSb precursor deposition, which is difficult to apply to large area substrates. Koswaththage *et al.* also investigated crystallization of InSb films on glass substrates by blue laser diode annealing (BLDA), where the InSb precursor films were deposited by sputtering, and reported carrier mobility of 1050 $cm^2 V^{-1} s^{-1}$ for grown films.[27] However, distinct crystallization results of sputter-deposited films on glass substrates using RTA have been hardly reported yet.

In the present study, we investigate the crystallization of sputter-deposited InSb films on low-cost glass substrates by RTA.

Published under an exclusive license by AIP Publishing

Through optimization of sputtering and RTA conditions, polycrystalline InSb films, consisting of very large crystal domains, having high carrier mobility (~10 000 $cm^2 V^{-1} s^{-1}$ at 300 K) are obtained.

II. EXPERIMENTAL PROCEDURE

InSb precursor films (thickness: 300–1000 nm) were deposited on glass substrates at room temperature by RF magnetron sputtering of an InSb alloy target (In:Sb = 50:50, purity: 99.99%) with an Ar plasma under various conditions (RF power: 100 W, pressure: 1.5–4.5 Pa, the distance between target and substrate: 70–100 mm, deposition rate: 0.3–1.3 nm/s). The base pressure of the sputtering system was 2×10^{-5} Pa. Subsequently, SiO_2 capping layers (thickness: 50 nm) were deposited by RF magnetron sputtering of a SiO_2 target (purity: 99.99%) in the same chamber with an Ar plasma (RF power: 200 W, pressure: 0.5 Pa, the distance between target and substrate: 70 mm, deposition rate: 0.4 nm/s) to suppress the evaporation of Sb from the InSb films.[26] The samples were annealed at a temperature between 200 °C and 500 °C for 1 min by RTA in N_2 ambience. The annealing temperature was monitored using a thermocouple attached to the sample stage. The deviation of the temperature was within ±5 °C during the annealing.

The growth features, composition, crystallinity, and electrical properties of the samples were investigated using Nomarski optical microscopy, energy dispersive x-ray spectroscopy of scanning electron microscopy (SEM-EDX) (acceleration voltage: 10 kV), microprobe Raman scattering spectroscopy (laser spot diameter: ~1 μm, wavelength: 532 nm, laser power: 200 mW), and Hall effect measurements (magnetic field: 0.05–0.55 T). The crystal structures and composition profiles of the grown samples were analyzed using electron backscattering diffraction (EBSD), cross-sectional transmission electron microscopy (TEM), and EDX mapping of TEM (TEM-EDX mapping).

III. RESULTS AND DISCUSSIONS

For the initial trial, we examine the crystallization of InSb precursor films deposited by sputtering (RF power: 100 W, pressure: 1.5 Pa, the distance between target and substrate: 70 mm, deposition rate: 1.3 nm/s). Figures 1(a) and 1(b) show typical Nomarski micrographs of samples (thickness: 300 nm) before and after RTA (490 °C, 1 min). Before RTA, a very flat and smooth surface is observed. However, the InSb film becomes rough and is partially lost by evaporation although the RTA temperature (490 °C) is below the melting point of InSb (525 °C).[28] To clarify the reason for the evaporation, we investigate the composition of the sample using SEM-EDX. The measurements revealed that the In/Sb ratio in the InSb precursor films before RTA was about 1.0. However, Ar with about 1% was included in the InSb precursor films. This fact suggests that the partial evaporation of the InSb films during RTA should be induced by Ar incorporation in the films.

For the suppression of InSb evaporation during RTA, we examine decrease of Ar incorporation in the deposited InSb films. It is speculated that reduction of the incident energy and the flux of Ar ions irradiated to the depositing InSb films should decrease the Ar incorporation in the InSb precursor films. Thus, we increase the pressure during sputtering from 1.5 to 4.5 Pa and the distance between the target and the substrates from 70 to 100 mm, where the RF power is 100 W, and the deposition rate is 0.3 nm/s. Figures 2(a)–2(f) show Nomarski micrographs of samples (thickness: 300 nm) before and after RTA (200 °C–490 °C, 1 min). These figures indicate that the film evaporation is effectively suppressed even after RTA at 490 °C under the new sputtering conditions. The SEM-EDX measurements for the samples revealed that Ar concentration was decreased to about 0.3%. These results show that the film evaporation, as shown in Fig. 1(b) is suppressed by decreasing Ar incorporation in the deposited films. Thus, we adopt this sputtering condition in the following experiments of the present study. It is noted that the In/Sb ratio in the as-deposited InSb films was slightly increased to about 1.1. This increase should be due to change in the sputtering yields of In and Sb atoms under this sputtering condition.

We investigate the crystallinity of the samples using microprobe Raman scattering spectroscopy. The Raman spectra for samples (thickness: 300 nm) before and after RTA are summarized in Fig. 2(g) as a function of the RTA temperature. Raman peaks due to transverse optical (TO) and longitudinal optical (LO) phonon modes of crystalline InSb[29] are weakly observed even for the sample before RTA, which indicates that a small fraction of crystalline InSb is produced during sputtering at room temperature due to energy supplied from the plasma. After RTA, the intensities of these Raman peaks are increased. Especially, for RTA temperatures above 400 °C, a significant increase in the Raman peaks is observed, which suggests that crystallization of the sputter-deposited InSb films significantly proceeds at temperatures above 400 °C.

The electrical properties of the grown films are studied using Hall effect measurements. The measurements show that the grown samples are n-type, which is attributed to donor levels due to native defects such as Sb antisites and In vacancies[30,31] and unintentionally incorporated Si and O atoms in InSb films.[32] Carrier mobilities and carrier concentrations of samples (thickness:

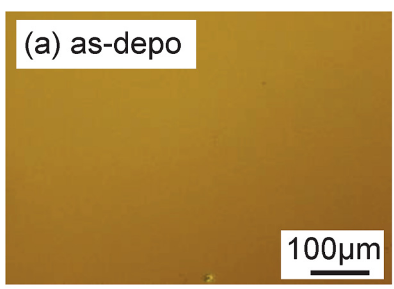

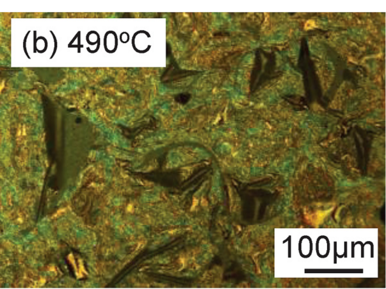

FIG. 1. Nomarski micrographs of samples (thickness: 300 nm) before (a) and after RTA (490 °C, 1 min) (b). The InSb films were deposited by sputtering (RF power: 100 W, pressure: 1.5 Pa, the distance between target and substrate: 70 mm, deposition rate: 1.3 nm/s).

Published under an exclusive license by AIP Publishing

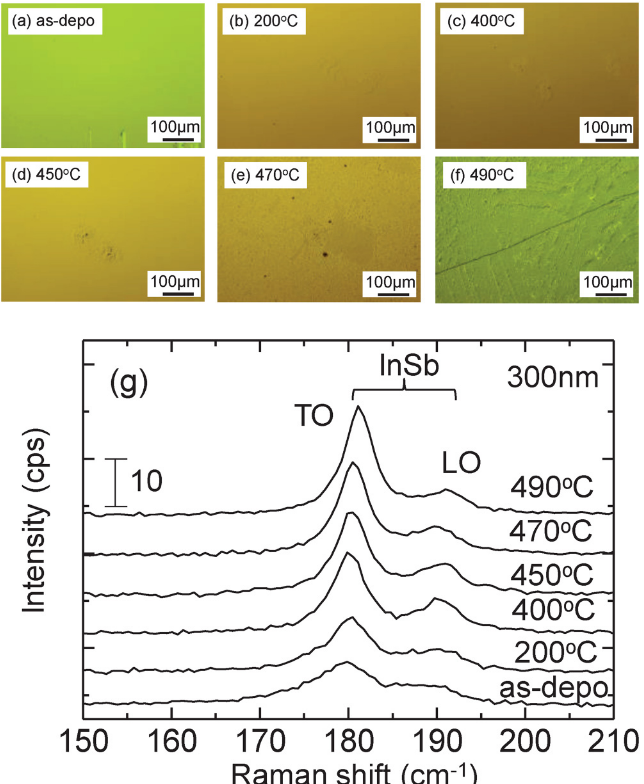

FIG. 2. Nomarski micrographs of samples (thickness: 300 nm) before (a) and after RTA at 200 °C (b), 400 °C (c), 450 °C (d), 470 °C (e), and 490 °C (f) for 1 min and Raman spectra obtained from samples before and after RTA (200 °C–490 °C, 1 min) (g). The InSb films were deposited by sputtering under modified conditions, i.e., RF power: 100 W, pressure: 4.5 Pa, the distance between target and substrate: 100 mm, and deposition rate: 0.3 nm/s.

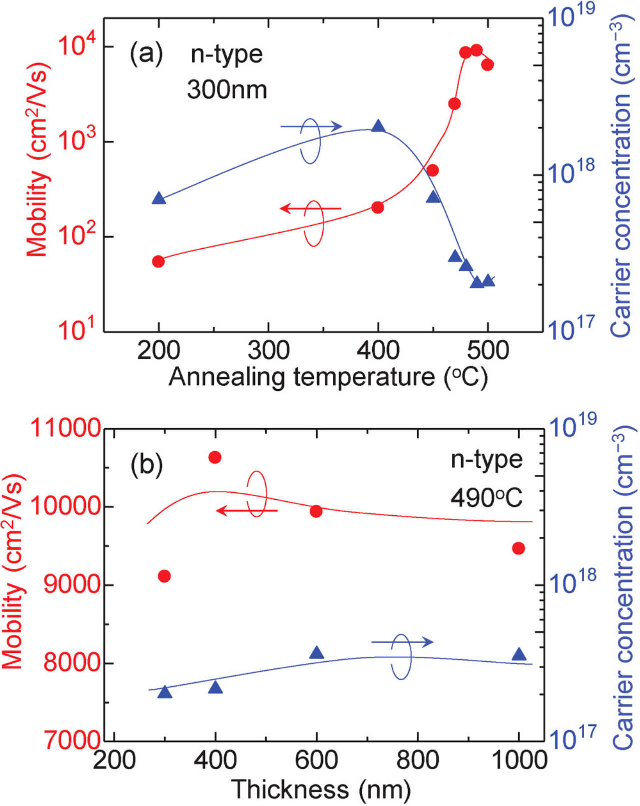

FIG. 3. RTA temperature dependence of carrier mobility and carrier concentration of samples (thickness: 300 nm, RTA time: 1 min) (a) and film thickness dependence of carrier mobility and carrier concentration of samples grown by RTA (490 °C, 1 min) (b).

300 nm) at room temperature obtained by Hall effect measurements with a magnetic field of 0.55 T are summarized in Fig. 3(a), as a function of the RTA temperature. It is noted that carrier mobilities and carrier concentrations obtained by Hall effect measurements of the grown films did not depend on the magnetic fields in the range of 0.05–0.55 T. As shown in Fig. 3(a), the carrier mobilities significantly increase with increasing RTA temperature from 200 to 490 °C and shows a maximum value of 9100 $cm^2 V^{-1} s^{-1}$ at 490 °C, and then the mobilities decrease at temperatures above 490 °C. On the other hand, the carrier concentrations increase with increasing RTA temperature from 200 to 400 °C and show a maximum value of $2.0 \times 10^{18} cm^{-3}$ at 400 °C. For RTA temperatures above 400 °C, the carrier concentrations decrease and show a minimum of $2.0 \times 10^{17} cm^{-3}$ at 490 °C. The increase in the carrier mobilities and decrease in the carrier concentrations above 400 °C are attributed to the progress of crystallization of the InSb films, as suggested from the Raman measurement results shown in Fig. 2(g). On the other hand, no morphological or crystallinity changes were detected for the samples after RTA at 500 °C (not shown), and thus, the reason for the decrease in the carrier mobilities for RTA temperatures of 500 °C is not clear. As a result, very high carrier mobility of 9100 $cm^2 V^{-1} s^{-1}$ is obtained by RTA at 490 °C for the film thickness of 300 nm.

Thickness dependence of electrical properties is examined for samples (thickness: 300–1000 nm) grown by RTA at 490 °C for 1 min. The carrier mobilities and concentrations are summarized as a function of the film thickness in Fig. 3(b). The figure shows that very high carrier mobilities (9000–10 000 $cm^2 V^{-1} s^{-1}$) are obtained for samples with a wide range of thickness (300–1000 nm). Although reported data of InSb films deposited by sputtering are very limited,[27] the high carrier mobilities obtained in the present study suggest that the sputtering technique should be useful to obtain high-carrier mobility InSb films on large-area glass substrates at low costs.

Crystal structures of grown InSb films are investigated using EBSD, where the capping SiO_2 layers were removed by wet etching with a diluted HF aqueous solution before the EBSD measurements. The measurements revealed that no Kikuchi patterns were detected for samples grown at temperatures below 400 °C, though crystal structures were recognized for RTA temperatures above

Published under an exclusive license by AIP Publishing

450 °C. Figures 4(a) and 4(b) show EBSD images of the sample (thickness: 300 nm) after RTA at 470 °C for 1 min, which indicate crystal orientations normal (z axis) and in-plane (x axis), respectively, to the sample surface. These figures indicate that the InSb layer grown at 470 °C dominantly consists of randomly oriented small crystal grains (∼5 μm). It is noted that a few (111)-oriented long regions (width: ∼5 μm, length: ≥15 μm) are also observed in Fig. 4(a).

EBSD images of the sample after RTA at 490 °C for 1 min are shown in Figs. 4(c) and 4(d), indicating crystal orientations normal (z axis) and in-plane (x axis), respectively, to the sample surface. These figures indicate that the InSb layer grown at 490 °C consists of fairly large domains (>100 μm) preferentially oriented to (111). It is noted that the RTA temperature (490 °C) is close to the melting point of InSb (525 °C). For the case of poly-Si, it was reported that regrowth of small crystal grains occurred during annealing at high temperatures (1350–1400 °C) closed to the melting point of Si (1414 °C).[33,34] We speculate that the large crystal domains observed after RTA at 490 °C are obtained by the regrowth of randomly oriented small grains as shown in Fig. 4(a), where (111)-oriented grains should be energetically favorable on glass substrates[35] and act as the seeding crystals for the regrowth. The (111)-oriented long regions observed in Fig. 4(a) should be the intermediate products during the regrowth.

Although (111)-oriented large domains (>100 μm) are observed in Fig. 4(c), we can observe small domains with different in-plane orientations in Fig. 4(d). To reveal the phenomena, a magnified image of the area indicated by the rectangular area in Fig. 4(c) is shown in Fig. 4(e), where the red and black lines show the Σ3 coincidence-site-lattice boundaries (twin boundaries) and random boundaries, respectively.

Detailed structures of the grown InSb films are studied using TEM. Figures 5(a) and 5(b) show the bright-field and dark-field images, respectively, of the sample (thickness: 300 nm) after RTA (490 °C, 1 min), where the capping SiO_2 layer was removed before the TEM observation. The dark-field image indicates that the whole area of the InSb film in this image consists of an almost

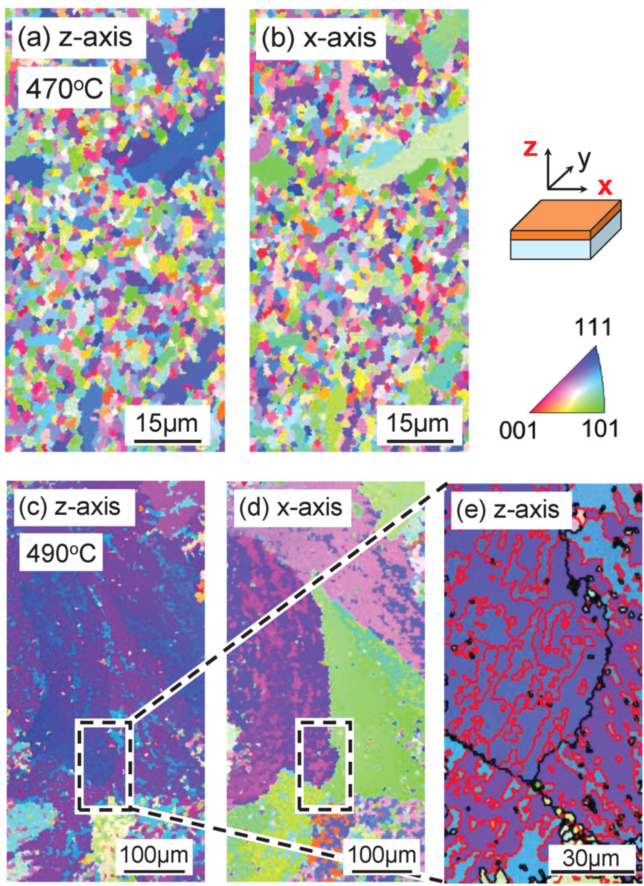

FIG. 4. EBSD images of samples (thickness: 300 nm) grown by RTA at 470 °C [(a) and (b)] and 490 °C [(c)–(e)] for 1 min. [(a), (c), and (e)] and [(b) and (d)] indicate crystal orientations normal and in-plane, respectively, to the sample surfaces. The rectangular area shown in (c) is magnified in (e). Red and black lines in (e) show the Σ3 coincidence-site-lattice boundaries (twin boundaries) and random boundaries, respectively.

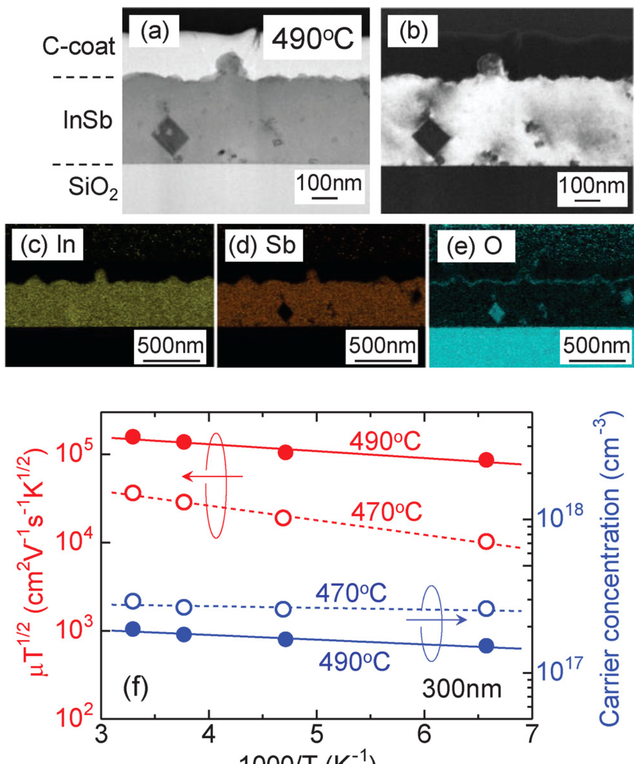

FIG. 5. TEM bright- (a) and dark-field images (b), TEM-EDX mapping of In (c), Sb (d), and O (e) of sample (thickness: 300 nm) grown by RTA (490 °C, 1 min), and Arrhenius plots of $\mu T^{1/2}$ and carrier concentration (f) of samples (thickness: 300 nm) grown by RTA at 470 °C (open circles) and 490 °C (closed circles) for 1 min.

Published under an exclusive license by AIP Publishing

single crystal. However, it is found that the InSb layer in the bright-field image contains small square-shaped inclusions. TEM-EDX mapping of In, Sb, and O elements are shown in Figs. 5(c)–5(e), respectively. These results indicate that the small square inclusions consist of In and O. From the detailed analysis of selected area electron diffraction patterns, it was revealed that the small square inclusions were In_2O_3 crystals. Some research groups reported that the In oxide is easily formed by the oxidation of InSb.[36] Thus, it is speculated that O atoms supplied from the SiO_2 capping layer should form In_2O_3 by selective oxidation of In in the InSb film during RTA. The TEM images shown in Fig. 5 indicate that the surface of the grown InSb film is rough. Menon *et al.* reported that In droplets (melting point: 157 °C) in In-rich InSb films should cause morphological changes of InSb films during annealing.[37] Thus, the surface roughening of the InSb film, as well as the formation of In_2O_3 inclusions, observed in Fig. 5 can be attributed to excess In in the film, whose In/Sb ratio is about 1.1. It is noted that Si atoms are hardly detected in the grown layer by the TEM-EDX measurements (not shown).

To clarify the electrical properties of grain boundaries of grown InSb films, we analyze carrier transport using a model proposed by Seto, which was originally developed for poly-Si.[38] Mobility μ of polycrystalline semiconductors is expressed by the following equation:[38]

$$\mu = \frac{Lq}{\sqrt{2\pi m^* kT}} \exp\left(-\frac{E_B}{kT}\right), \tag{1}$$

where L is the crystal grain size, q is the elementary charge, m^* is the effective mass of the carrier, k is the Boltzmann constant, T is the absolute temperature, and E_B is the energy barrier height at grain boundaries. Here, energy barrier height E_B is generated by trapping states with density Q_t at grain boundaries, and given by the following equation:[38]

$$E_B = \frac{qQ_t^2}{8\varepsilon N}, \tag{2}$$

where ε is the dielectric constant of the semiconductor and N is the carrier concentration.

Arrhenius plots of $\mu T^{1/2}$ and carrier concentration of the sample (thickness: 300 nm) grown by RTA (490 °C, 1 min) are shown by the closed circles in Fig. 5(f). In the figure, the data of the sample (thickness: 300 nm) grown at 470 °C are also shown by the open circles for comparison. Respective data are fitted with straight lines. From the slopes for $\mu T^{1/2}$, the values of the energy barrier height E_B are evaluated as 33 meV (RTA temperatures: 470 °C) and 16 meV (490 °C) using Eq. (1), and the values of the trapping state density Q_t are evaluated as 8.4×10^{11} cm^{-2} (470 °C) and 4.7×10^{11} cm^{-2} (490 °C) from E_B using Eq. (2). The values of E_B and Q_t are much smaller compared to conventional semiconductor materials such as poly-Si grown by chemical-vapor deposition,[38] but similar to poly-Si[39] and poly-Ge[40] obtained by solid-phase crystallization, which show higher carrier mobilities. On the other hand, the values of the activation energy of the carrier concentration were evaluated as 2.2 and 6.2 meV for samples grown at 470 and 490 °C, respectively. Since all of the shallow donors in the InSb films should be completely electrically activated at the measurement temperatures of 150–300 K, it is suggested that the values of the activation energy should not correspond to the energy levels of the shallow donors. Further investigation is needed to clarify the details of the activation energy of the carrier concentration.

Using Eq. (1), the values of the crystal grain size L are evaluated as 8.1 μm (470 °C) and 18.0 μm (490 °C). For the sample grown at 470 °C, the value (8.1 μm) shows a good agreement with that (~5 μm) obtained by the EBSD analysis shown in Figs. 4(a) and 4(b). On the other hand, the value (18.0 μm) for the sample grown at 490 °C is much smaller compared with the size (>100 μm) of domains defined by the random boundaries indicated by the black lines in Fig. 4(e). Instead, it agrees well with the size (~20 μm) of sub-domains defined by the Σ3 boundaries (twin boundaries), indicated by the red lines in Fig. 4(e). This suggests that the carrier transport in the sample grown at 490 °C should be limited by carrier scattering at the sub-domain boundaries, i.e., Σ3 boundaries (twin boundaries), whose barrier heights are smaller compared with the random grain boundaries.

From these results, it is clarified that the poly-InSb films obtained in the present study show high carrier mobilities, because the films consist of the (111)-oriented large domains (>100 μm) having sub-domains of twins with low barrier heights at the sub-domain boundaries.

IV. CONCLUSION

The formation of poly-InSb films on low-cost glass substrates by RTA has been investigated using sputter-deposited InSb films. By tuning the sputtering conditions, the incorporation of Ar into the InSb films was decreased. This decrease in the Ar content effectively suppressed the evaporation of the films during RTA. The crystallization of InSb films significantly proceeded by RTA at temperatures above 400 °C. With increasing RTA temperature, the carrier mobilities were increased, while the carrier concentrations were decreased. As a result, InSb films (thickness: 300–1000 nm) having high carrier mobilities of 9000–10 000 cm^2 V^{-1} s^{-1} were obtained by RTA at 490 °C for 1 min. These high carrier mobilities of the poly-InSb films are attributed to (111)-oriented large crystal domains (>100 μm), consisting of twins with a low barrier height (16 meV) at the twin-boundaries. This technique employing sputtering and RTA will be useful for fabricating InSb-based advanced devices with low production costs.

ACKNOWLEDGMENTS

The authors wish to thank Mr. S. Yoshitome and Mr. M. Sakai of e-tec Inc. for valuable discussions and suggestions in the course of the study and Professor T. Asano of Kyushu University for providing the opportunity to use the EBSD analysis system. Part of this work was supported by JST A-STEP Grant No JPMJTM20GV and a Grant-in-Aid (No. JP22K04186) for Scientific Research from the Ministry of Education, Culture, Sports, Science and Technology in Japan.

Published under an exclusive license by AIP Publishing

AUTHOR DECLARATIONS

Conflict of Interest

The authors have no conflicts to disclose.

Author Contributions

Takashi Kajiwara: Data curation (equal); Formal analysis (equal); Investigation (equal); Methodology (equal); Writing – review & editing (equal). **Otokichi Shimoda:** Data curation (equal); Formal analysis (equal); Investigation (equal); Methodology (equal). **Tatsuya Okada:** Conceptualization (equal); Data curation (equal); Formal analysis (equal); Funding acquisition (equal); Investigation (equal); Methodology (equal); Project administration (equal); Supervision (equal); Writing – review & editing (equal). **Charith Jayanada Koswaththage:** Conceptualization (equal); Formal analysis (equal); Investigation (equal); Methodology (equal); Writing – review & editing (equal). **Takashi Noguchi:** Conceptualization (equal); Formal analysis (equal); Funding acquisition (equal); Investigation (equal); Methodology (equal); Project administration (equal); Resources (equal); Supervision (equal); Writing – review & editing (equal). **Taizoh Sadoh:** Conceptualization (equal); Funding acquisition (equal); Investigation (equal); Methodology (equal); Project administration (equal); Resources (equal); Supervision (equal); Writing – original draft (equal); Writing – review & editing (equal).

DATA AVAILABILITY

The data that support the findings of this study are available from the corresponding author upon reasonable request.

REFERENCES

[1]O. Madelung, *Semiconductors Data Handbook*, 3rd ed. (Springer, Berlin, 2004), pp. 154–161.
[2]H. A. Nilsson, P. Caroff, C. Thelander, M. Larsson, J. B. Wagner, L.-E. Wernersson, L. Samuelson, and H. Q. Xu, Nano Lett. **9**, 3151–3156 (2009).
[3]S. A. Solin, D. R. Hines, A. C. H. Rowe, J. S. Tsai, Y. A. Pashkin, S. J. Chung, N. Goel, and M. B. Santos, Appl. Phys. Lett. **80**, 4012–4014 (2002).
[4]K. Togawa, H. Sanbonsugi, A. Lapicki, M. Abe, H. Handa, and A. Sandhu, IEEE Trans. Magn. **41**, 3661–3663 (2005).
[5]B. Madon, J.-E. Wegrowe, H.-J. Drouhin, X. Liu, J. Furdyna, and G. A. Khodaparast, J. Appl. Phys. **119**, 025701 (2016).
[6]G. K. Perkins, M. Kustov, E. Lovell, M. V. Pettifer, and L. F. Cohen, Rev. Sci. Instrum. **89**, 065111 (2018).
[7]S. J. Kim, S.-W. Lee, J. D. Song, Y.-W. Kwon, K.-J. Lee, and H. C. Koo, Sens. Actuators B: Chem. **255**, 2894–2899 (2018).
[8]Z. Chu, M. Fu, J. Guo, W. Wang, J. Zhou, X. Ma, and J. Guo, IEEE Trans. Biomed. Circuits Syst. **15**, 171–176 (2021).
[9]A. Rogalski, Prog. Quantum Electron. **27**, 59–210 (2003).
[10]K. W. Hodapp, J. B. Jensen, E. M. Irwin, H. Yamada, R. Chung, K. Fletcher, L. Robertson, J. L. Hora, D. A. Simons, and W. Mays, Publ. Astron. Soc. Pacific **115**, 1388–1406 (2003).
[11]G. H. Rieke, Annu. Rev. Astron. Astrophys. **45**, 77–115 (2007).
[12]S. Zhang, H. Jiao, X. Wang, Y. Chen, H. Wang, L. Zhu, W. Jiang, J. Liu, L. Sun, T. Lin, H. Shen, W. Hu, X. Meng, D. Pan, J. Wang, J. Zhao, and J. Chu, Adv. Funct. Mater. **30**, 2006156 (2020).
[13]M. Shimatani, S. Fukushima, S. Okuda, and S. Ogawa, Appl. Phys. Lett. **117**, 173102 (2020).
[14]M. Radosavljevic, T. Ashley, A. Andreev, S. D. Coomber, G. Dewey, M. T. Emeny, M. Fearn, D. G. Hayes, K. P. Hilton, M. K. Hudait, R. Jefferies, T. Martin, R. Pillarisetty, W. Rachmady, T. Rakshit, S. J. Smith, M. J. Uren, D. J. Wallis, P. J. Wilding, and R. Chau, in *IEEE International Electron Devices Meeting Technical Digest* (IEEE, 2008), p. 727.
[15]H. A. Nilsson, P. Caroff, C. Thelander, E. Lind, O. Karlström, and L.-E. Wernersson, Appl. Phys. Lett. **96**, 153505 (2010).
[16]Ö Gül, D. J. van Woerkom, I. van Weperen, D. Car, S. R. Plissard, E. P. A. M. Bakkers, and L. P. Kouwenhoven, Nanotechnology **26**, 215202 (2015).
[17]B. Dalelkhan, D. J. O. Göransson, C. Thelander, K. Li, Y. J. Xing, V. F. Maisi, and H. Q. Xu, Nanoscale **12**, 8159–8165 (2020).
[18]V. Mourik, K. Zuo, S. M. Frolov, S. R. Plissard, E. P. A. M. Bakkers, and L. P. Kouwenhoven, Science **336**, 1003–1007 (2012).
[19]A. Das, Y. Ronen, Y. Most, Y. Oreg, M. Heiblum, and H. Shtrikman, Nat. Phys. **8**, 887–895 (2012).
[20]M. T. Deng, C. L. Yu, G. Y. Huang, M. Larsson, P. Caroff, and H. Q. Xu, Nano Lett. **12**, 6414–6419 (2012).
[21]S. Salimian, M. Carrega, I. Verma, V. Zannier, M. P. Nowak, F. Beltram, L. Sorba, and S. Heun, Appl. Phys. Lett. **119**, 214004 (2021).
[22]A. Okamoto and I. Shibasaki, J. Cryst. Growth **251**, 560–564 (2003).
[23]I. Shibasaki, H. Geka, and A. Okamoto, J. Cryst. Growth **311**, 1696–1699 (2009).
[24]J. Li, C. Tang, P. Du, Y. Jiang, Y. Zhang, X. Zhao, Q. Gong, and X. Kou, Appl. Phys. Lett. **116**, 122102 (2020).
[25]H. Menon, L. Södergren, R. Athle, J. Johansson, M. Steer, I. Thayne, and M. Borg, Nanotechnology **32**, 165602 (2021).
[26]C. J. Koswaththage, T. Okada, T. Noguchi, S. Taniguchi, and S. Yoshitome, AIP Adv. **6**, 115303 (2016).
[27]C. J. Koswaththage, T. Higashizako, T. Okada, T. Sadoh, M. Furuta, B. S. Bae, and T. Noguchi, AIP Adv. **9**, 045009 (2019).
[28]T. B. Massalski, *Binary Alloy Phase Diagrams* (American Society for Metals, Metals Park, 1986), Vol. 2, p. 1395.
[29]W. Kiefer, W. Richter, and M. Cardona, Phys. Rev. B **12**, 2346–2354 (1975).
[30]A. Höglund, C. W. M. Castleton, M. Göthelid, B. Johansson, and S. Mirbt, Phys. Rev. B **74**, 075332 (2006).
[31]J. Buckeridge, T. D. Veal, C. R. A. Catlow, and D. O. Scanlon, Phys. Rev. B **100**, 035207 (2019).
[32]Z. Yuanxi, in *Semiconductors and Semimetals*, edited by R. K. Willardson and A. C. Beer (Academic Press, San Diego, 1988), Vol. 26, Chap. 1, p. 29.
[33]C. Daey Ouwens and H. Heijligers, Appl. Phys. Lett. **26**, 569–571 (1975).
[34]W. J. H. Schins, J. Bezemer, H. Holtrop, and S. Radelaar, J. Electrochem. Soc. **127**, 1193–1199 (1980).
[35]R. J. Jaccodine, J. Electrochem. Soc. **110**, 524 (1963).
[36]C. W. Wilmsen, Thin Solid Films **39**, 105–117 (1976).
[37]H. Menon, N. P. Morgan, C. Hetherington, R. Athle, M. Steer, I. Thayne, A. Fontcuberta i Morral, and M. Borg, Phys. Status Solidi (A) **219**, 2100467 (2022).
[38]J. Y. W. Seto, J. Appl. Phys. **46**, 5247–5254 (1975).
[39]T. Noguchi and Y. Kanaishi, IEEE Electron Device Lett. **10**, 543–546 (1989).
[40]C. Xu, X. Gong, M. Miyao, and T. Sadoh, Appl. Phys. Lett. **115**, 042101 (2019).

Published under an exclusive license by AIP Publishing